3. PARTICIPATION IN THE USE OF THE JET FACILITIES BY THE EFDA ASSOCIATES

F. Serra (Head), D. Alves, P. Belo, D. Borba, R. Coelho, S. Cortes, N. Cruz, L. Cupido, L. Fattorini, A. Figueiredo, B. Gonçalves, S. Hacquin, M.E. Manso, L. Meneses, F. Nabais, M.F. Nave, I. Nedzelski, I. Nunes, V. Plyusnin, T. Ribeiro, F. Salzedas, C. Silva, J. Sousa, C. Varandas, P. Varela.

3.1. INTRODUCTION

The Association EURATOM/IST has proceeded with its participation in the collective use of the JET[1] Facilities, in the frame of the "European Fusion Development Agreement" (EFDA), through the "JET Operation Contract" and the "JET Implementing Agreement".

This chapter presents the main activities carried out during this year in the areas of:

- Operation;
- Scientific exploitation;
- Performance enhancements;
- Management.

3.2. OPERATION

Three members of the IST/CFN staff have been involved in the JET operation: Drs. Sebastien Hacquin and Isabel Nunes have participated in the JET Operation Team, through Secondment Agreements with the Association EURATOM/UKAEA, working respectively in the "Electron Kinetics Group" and "Operation Group"; Mr. Luis Meneses has provided technical support to the operation and maintenance of the KG8 correlation reflectometer.

3.3. SCIENTIFIC EXPLOITATION

3.3.1. Introduction

The participation in the JET 2004 Work Programme had contributions from fifteen scientists to the experimental campaigns C13 and C14 at the JET site (Table 3.1).

The work has been focused on code developments, leading to the following studies and/or tasks in plasma physics and/or engineering mainly related with Task Forces M, D and E: (i) Study of the sawtooth stability in plasmas with counter-NBI; (ii) Expansion of the JET sawtooth database; (iii) Validation of q-profiles in JET optimised shear discharges; (iv) Documentation of JET diagnostics for analysis of fluctuations; (v) Stability domains for the internal kink mode; (vi) Limiter H-mode studies in JET; (vii) Evidence of fast ion redistribution during fishbones from TAE in JET deuterium plasmas; (VIII) Transport studies in Tritium plasmas; (ix) Time–frequency analysis of non-stationary fusion plasma signals by comparison between the Choi–Williams distribution and wavelets; (x) Disruptions and runaway electrons in JET; (xi) Effects of large magnetic islands on particle confinement trace-Tritium studies (TRANSP modelling); (xii) Cross-correlation between parallel and radial fluctuating velocities; (xiii) Design of a new reciprocating probe head; (xiv) Studies of MHD and turbulence based on microwave reflectometry results.

Name	Competence	Number of days
Duarte Borba	TFL, MHDAE	47
M. Filomena Nave	TSL, SL, MHDAE	52
Paula Belo	IEMHDA, CATS	47
Fernando Nabais	FPE	47
Vladislav Plyusnin	MHDME	33
Carlos Silva	KY3	19
Isabel Nunes	KG8b	26
Jorge Ferreira	PTM	26
Igor Nedzelski	KY3	26
Luis Meneses	KG8b	12
Ricardo Galvão	MHDAE	32
Sebastien Hacquin	JOC	20

Table 3.1 – IST/CFN staff envolved in the JET experimental campaigns

3.3.2. Study of the sawtooth stability in plasmas with counter-NBI

During a recent reversed toroidal field (B_T) campaign at JET, experiments were performed to investigate the effect on sawteeth of NBI-driven toroidal plasma rotation counter to the direction of the toroidal plasma current (I_p) and B_T. A power scan at constant density has permitted comparison of the reverse B_T domain with previous experiments with forward field and hence co-rotation. Unlike observations with co-NBI heating where the sawtooth period increases with power, with counter-NBI the sawtooth period was found to decrease to a minimum value (about 1/3 of Ohmic sawtooth periods) at 4 MW (Figure 3.1). The possible reasons why the sawtooth period is shorter with counter-NBI are under investigation. In earlier JET experiments with reversed B_T and I_p plasmas this was attributed to changes in the q-profile due to neutral beam current drive (NBCD). Modification in the core current density due to NBCD, j_{CD}, was calculated with the PENCIL code. j_{CD} was larger with counter-injection and increased with the input power (Figure 3.2). PENCIL calculations show that the fast ions pressure increased with power for both the usual and the reversed B_T cases. The lack of correlation between the observed sawtooth period and fast ion pressure in the counter-NBI case indicates that the

[1] JET is an European tokamak, operated and scientifically exploited in the frame of the European Fusion Development Agreement (EFDA).

contribution from the fast particle component cannot explain the observed sawtooth period dependence on P_{NBI}. On the other hand, kinetic effects from trapped thermal ions qualitatively explain the sawtooth observations. The effect of sheared flow on these kinetic effects modifies the stability threshold of the internal kink mode in such a way that the critical beta for instability is much lower for small or reversed toroidal rotation, as observed in the discharges with reversed B_T and I_P.

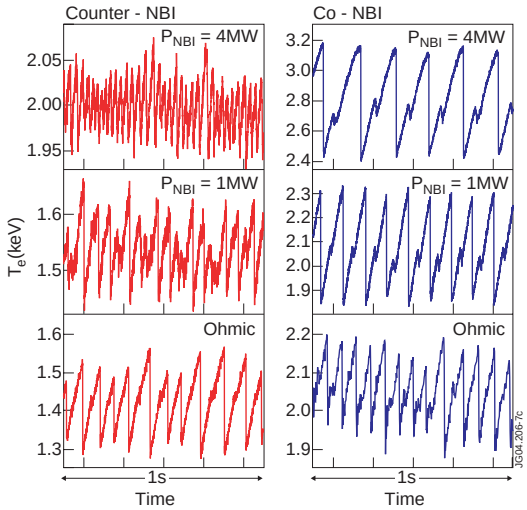

Figure 3.1 – Central electron temperature traces showing the different sawtooth behaviour for different input powers observed with co and counter NBI.

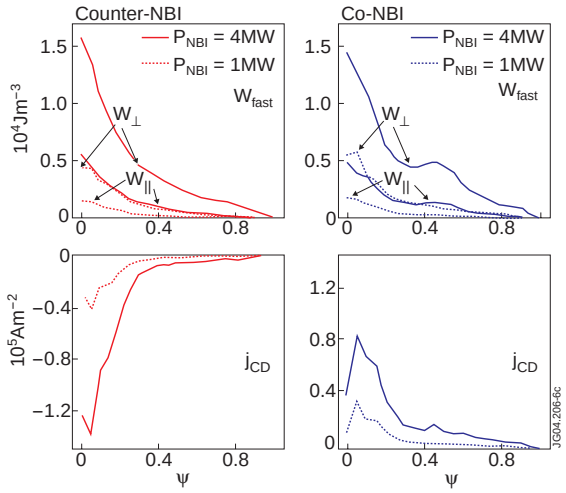

Figure 3.2 – (a) and (b) Profiles of fast ion energy density $W_{//fast}$ and $W_{\perp fast}$ calculated with the PENCIL code (finite orbit width effects neglected); (c) and (d) Profiles of driven current density ($j_{CD}/j_0 \leq 10\%$ for co- and counter-NBI).

3.3.3. Expansion of the JET Sawtooth Database

A sawtooth database, initiated during campaigns C1-C4 for the study of sawtooth observations in NBI heated discharges, has been expanded. The database now contains information on ICRH discharges including recent experiments on grassy sawteeth and some He plasmas. In addition, data from several TFE pedestal and divertor experiments performed during the reversed toroidal field campaign have been included. The database contains average plasma and heating parameters, as well as specific sawtooth characteristics.

Figure 3.3 shows a comparison of the sawtooth period versus the central electron temperature obtained for NBI heating with the usual JET B_T and I_p polarity (co-NBI) and with reversed B_T and I_p (counter-NBI). For co-NBI, the sawtooth period scales with $T_e^{1.7}$. This is not found for counter-NBI. The comparison confirms that sawtooth periods are generally smaller with counter-NBI for similar central T_e. Therefore tokamak operation with counter-NBI is an effective way to control the sawtooth period in H-mode as well as in L-mode plasmas. Figure 3.4 presents a plot of the sawtooth period versus the central electron temperature for NBI as well as ICRH discharges in the normal B_T and I_P operation. The open triangle symbols correspond to an interesting low density regime with ICRH that shows small sawteeth, referred to as the "grassy" sawtooth. Although auxiliary heating has been associated with sawtooth stabilization leading to large sawtooth periods, these figures clearly show that with either ICRH or with NBI heating there are regimes of operation where sawtooth periods shorter than in Ohmic plasmas can be obtained.

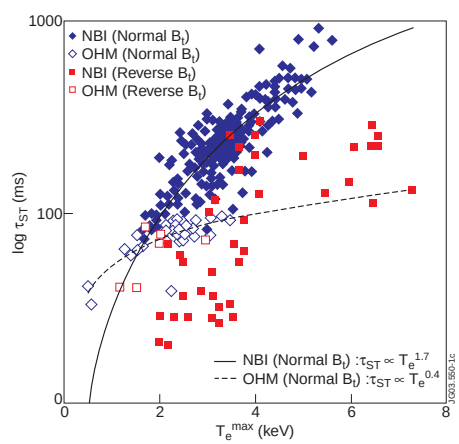

Figure 3.3 – A comparison of sawtooth periods with co-NBI (in solid blue kytes) and counter-NBI (red solid squares).

3.3.4. Validation of q-profiles in JET optimised shear discharges

A comparison of q-values obtained MHD analysis and q-profiles determined from EFIT with MSE measurements was performed for a set of discharges from the Trace Tritium Experiment (TTE). Alfvén Eigenmode (AE) cascades with frequencies ranging from 100-250 kHz can be identified with spectrograms from microwave signals in interferometry mode, as well as from magnetic signals.

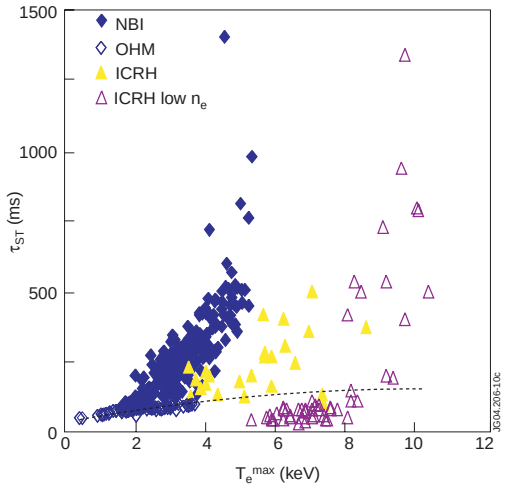

Figure 3.4 – A comparison of sawtooth periods in low-density ICRH pulses (open symbols) with observations in high density ICRH plasmas (solid yellow triangles) and NBI heated plasmas (blue solid kites).

In the case of reversed shear plasmas, the Alfvén cascades are used to determine the minimum of the safety factor (q_{min}).

The frequency pattern of the AE cascades reflects the time evolution of the Alfvén continuum at the location of q_{min} which is linked to the frequency of the eigenmode located at that surface. Measurements performed using the reflectometer diagnostic were able to detect eigenmodes with high toroidal mode numbers allowing more accurate determination of the (q_{min}) than with the magnetic diagnostic.

Figure 3.5 presents an example of q profile validation for a TTE discharge using MHD mode analysis. For the time shown, the AE analysis revealed a non-integer q_{min}~2.7-2.8. A snake with mode number m=3, n=1 indicated the presence of a integer q=3 surface. Figure 3.5 shows EFIT reconstructions of the q-profile with different fitting constraints. The EFIT reconstruction with magnetic data only (curve 1) is monotonic. Only the MSE data detects the current hole, however, the equilibrium reconstruction with MSE constrains shows a very large uncertainty in the plasma core. Clearly the MHD analysis is an important guide in selecting the optimum curvature of the fitted profiles.

3.3.5. Documentation of JET diagnostics for analysis of fluctuations

A set of fast magnetic pick-up coils was designed for high frequency MHD activity studies (up to 500 kHz). determination. A new data collection system (named KC1M) has been commissioned in 2004, allowing the magnetic signals to be recorded at 2 MHz for up to 32 s in each pulse. The system will be be enlarged to 32 magnetic MHD signals and 32 other selectable fast diagnostic signals in 2005. The ECE, SXR and O-mode reflectometer diagnostic measurements permit the identification of low amplitude, core MHD modes not measured by the external magnetic pick-up coils.

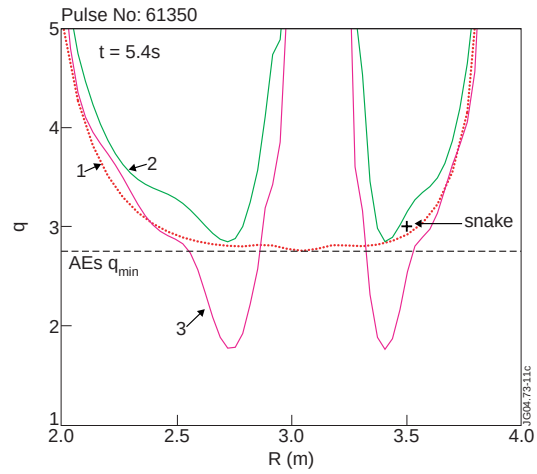

Figure 3.5 - q profile from EFIT with different boundary conditions: (1) magnetics only, (2) and (3) with magnetics and MSE data, fitting MSE data approximately (2) or very closely (3). Indicated in the figure is the estimated q_{min} from AE cascade analysis and the radius of q=3 obtained from the snake.

3.3.6. Stability domains for the internal kink mode

Fishbone and sawtooth activity are caused by different branches of the solution of the dispersion relation for the internal kink mode. The activity of these instabilities is governed mainly by three parameters, the growth rate of the ideal internal kink mode, $\gamma_I = -\omega_A \delta W_{MHD}$, the diamagnetic frequency ω_{*i} and the fast ions beta β_h. Following trends in the space of parameters ($\gamma_I, \omega_{*i}, \beta_h$), changes on sawtooth or fishbone activity occur when lines separating different stability regions for the internal kink mode are crossed.

To determine the stability domains for each instability in the space of parameters it is necessary to solve the marginal equation corresponding to the dispersion relation for the internal kink mode. The marginal equation produces two solutions if the ideal growth rate is below a maximum value $\gamma_I = \gamma_M$. The diagram containing these solutions in the space of parameters is presented in Figure 3.6 (red lines). It includes a (horizontal brown) line $\gamma_I = \omega_{*i}/2$ that indicates when the kink branch is stabilized by diamagnetic effects and to complete the stability regions, lines traducing resistive effects (at low values of γ_I) and finite orbit width effects (at large values of β_h) were also added to the diagram.

3.3.6.1. Fishbones cycle

Low-frequency (diamagnetic) fishbones are usually observed for low values of the fast ions beta while high-frequency (precessional) fishbones are observed only for high values of β_h. For intermediate values of β_h no fishbones are observed since it falls in the stable triangle of Figure 3.6. In recent experiments carried out with low-density plasmas, a new type of fishbones was observed.

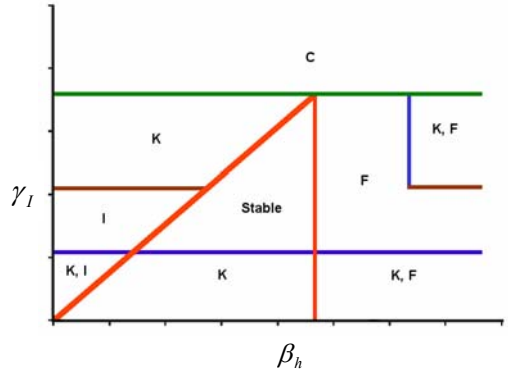

Figure 3.6 - Stability regions for the different branches of the internal kink mode in the space of parameters (the diamagnetic frequency determines the location of the red and brown lines). In the regions labelled with K, I and F the kink, ion and fishbone branches responsible for respectively sawteeth, low-frequency fishbones and high-frequency fishbones are unstables. For $\gamma_I > \gamma_M$ the low-frequency and high-frequency branches coalesce (region labelled with C).

These fishbones ranged all the way from high frequencies to low frequencies having characteristics of both diamagnetic and precessional fishbones, reason why were called hybrid fishbones. The fishbone behaviour was also observed to evolve during a sawteeth free period from high-frequency fishbones to low-frequency fishbones (Figure 3.7). Each hybrid fishbone corresponds to a single burst (Figure 3.8).

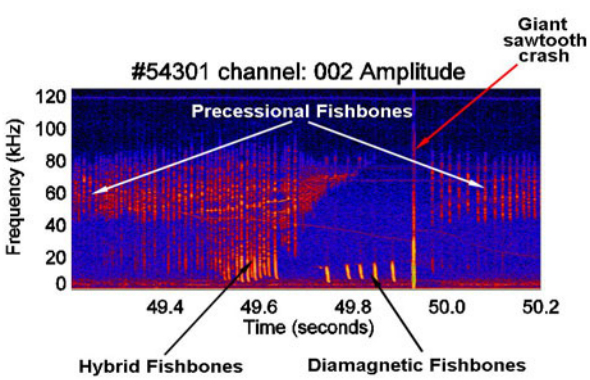

Figure 3.7 - Spectrogram of MHD activity for pulse #54301 showing the evolution of fishbone behaviour between sawtooth crashes.

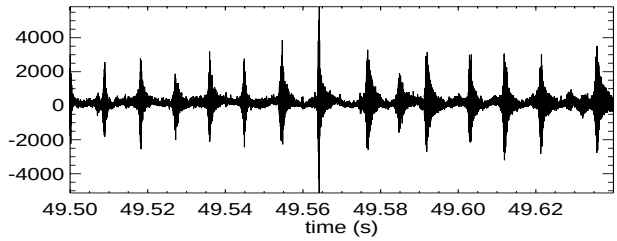

Figure 3.8 – Bursts of hybrid fishbones

At some point, hybrid fishbones begin chirping down only for a small range of frequencies becoming precessional fishbones and at the same time diamagnetic fishbones appear in the low frequencies. A new stage is reached where low amplitude bursts of both types of fishbones can be observed simultaneously. This occurs just before t=49.8 s. The precessional fishbones progressively disappear until only diamagnetic fishbones remain. A monster sawtooth crash occurs just after t=49.91 s and the fishbone activity is suppressed, but after a short time (t=50.0 s) precessional fishbones reappear.

3.3.6.2. Hybrid fishbones generating mechanism

The mechanism that produces this newly observed type of fishbones can be explained using the variational formalism.

The diamagnetic frequency (ω_{*i}) is mainly determined by the radial gradient of the background ions' pressure, so this means that when sawteeth are stabilized by fast ion effects, both γ_I and ω_{*i} increase. The effect of this increase in ω_{*i} over the stability diagram of Figure 3.9 is that the brown line ($\gamma_I = \omega_{*i}/2$) drifts upward and at the same time the green line ($\gamma_I = \gamma_M$) drifts downward. In these experiments the condition $\gamma_I < \omega_{*i}/2$ was reached first but the system remains in the same region of Figure 3.9 and only precessional fishbones are still observed.

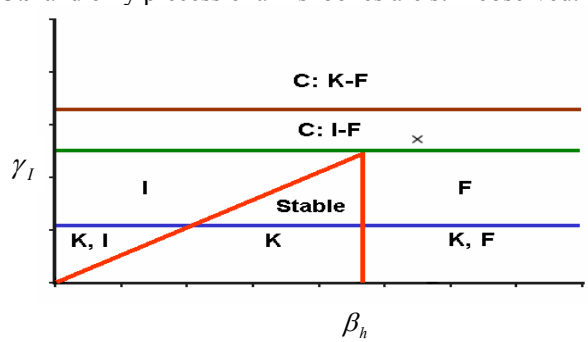

Figure 3.9 - Stability regions for the internal kink mode. In the regions labelled with K, I and F the kink, ion and fishbone branches are unstable. In the regions labelled with C:I-F and C:K-F the ion-fishbone and kink fishbone modes are unstable. The cross represents the state of the plasma when hybrid fishbones are observed.

After that, ω_{*i} continues to increase and at some point the condition $\gamma_I > \gamma_M$ is also reached. When this happens, the fishbone branch coalesces with the ion branch and a new region in the stability diagram is accessed (Figure 3.10).

The ion-fishbone branch is always unstable and, for a given value of ω_{*i}, behaves like the fishbone branch for high values of β_h and like the ion branch for lower values of β_h. If β_h is high enough when a fishbone burst is triggered, it begins as a precessional burst. During the burst fast particles are expelled from the plasma core and β_h decreases significantly. Thus, it is possible that β_h reaches values small enough for the mode behaviour change to that of a diamagnetic fishbone (Figure 3.10).

The result is that the fishbone that started as a precessional fishbone, accesses a new source of energy related to the bulk ions, that allows the amplitude of the oscillations to grow again, now with the characteristics of a diamagnetic fishbone with much slower oscillations in $\dot{\tilde{B}}_\theta$ (Figure 3.11). This mechanism produces hybrid fishbones which can only be observed when the coalescent ion-fishbone mode is unstable.

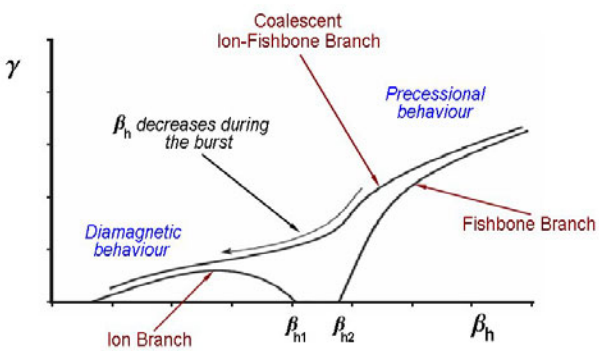

Figure 3.10 - Schematic diagram of the solution of the dispersion relation including diamagnetic and fast ion effects. The smaller arrow indicates the evolution of the mode behaviour during a hybrid burst, as fast ions are expelled from the plasma core and β_h decreases.

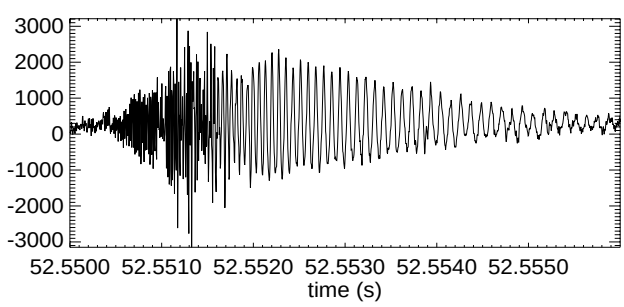

Figure 3.11 - Temporal evolution of $\dot{\tilde{B}}_\theta$ for the hybrid fishbone in pulse #54300.

3.3.7. Limiter H-mode studies in JET

Confinement transitions with the characteristics of H-mode were observed in JET inner wall limited plasmas in experiments performed at magnetic field of 0.8 T and at a current of 0.9 MA, using 5 MW of auxiliary heating power. The NBI heating is switched on for a period of 3 seconds (Figure 3.12), which is sufficient to achieve quasi steady state, given that both the overall energy confinement time and the beam slowing down time in these discharges are less than 200 ms. During this period several abrupt transitions in confinement are observed, which are characterised by a significant decrease in the H-alpha emission (Figure 3.13). However, limiter H-modes in JET are short lived (<20ms) and they are terminated by a burst of magnetic fluctuations with very similar characteristics to those of ELMs. The onset of the good confinement period is caused by a reduction in micro-turbulent transport very close to the plasma edge. On the other hand the termination of the period of good confinement has a clear magnetic signature, most likely caused by an edge instability driven by the steep pressure or current profiles.

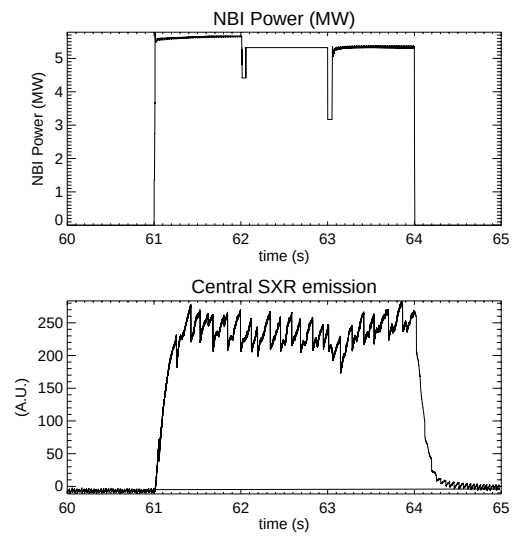

Figure 3.12 - Time evolution of NBI power for the limiter discharge #60908 and the central soft x-rays emission showing the Sawtooth.

3.3.8. Evidence of fast ion redistribution during fishbones from TAE in JET deuterium plasmas

TAEs were found to be unstable in JET limiter plasmas with B_t = 0.8 T and I_p = 0.9 MA. TAEs and large amplitude fishbones were destabilised by 5 MW of NBI. TAEs with toroidal mode numbers n=4, 5 and 6 were seen in the absence of fishbones, while n=2 and 3 TAEs appear in the presence of fishbones (Figures 3.14 and 3.15). This observation is consistent with a fishbone localised mainly inside q=1 redistributing fast ions and providing a steeper dp_{beam}/dr outside q=1. A steeper dp_{beam}/dr outside q=1 destabilises TAEs with lower n.

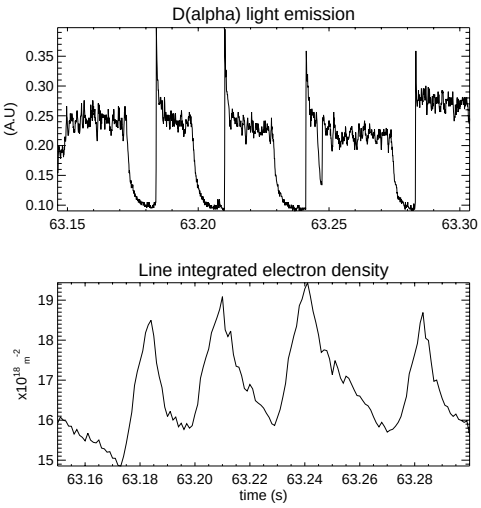

Figure 3.13 - D-alpha light emission and edge density (microwave interferometer) evolution during the H-mode transitions.

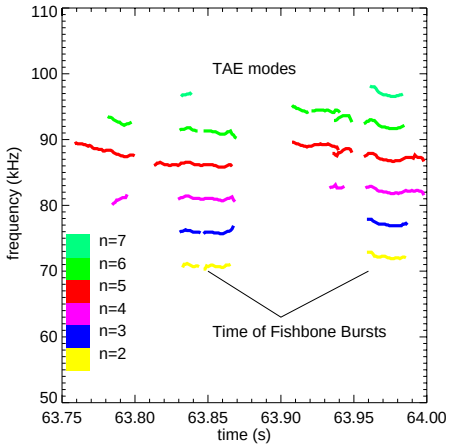

Figure 3.14 - TAE mode spectrum with different toroidal mode numbers (n), during the fishbone bursts.

3.3.9. Tritium transport studies

3.3.9.1. Modelling Tritium penetration

In recent JET campaigns, "trace" tritium gas puff was used in high performance discharges, to study the transport of a hydrogen isotope particle in high performance ELMy H-mode plasmas.

To model the trace tritium penetration, a 1.5D transport code JETTO was used. Tritium, being a minority species, is considered as low Z impurity for the neo-classical transport. NCLASS code was used for the neo-classical diffusion and convective velocity. For the anomalous particle diffusion the empirical model Bohm/GyroBohm was considered. For the anomalous convective velocity two theory motivated models are used in JETTO. This velocity is dependent on the magnetic shear or/and temperature gradient/Tritium boundary values.

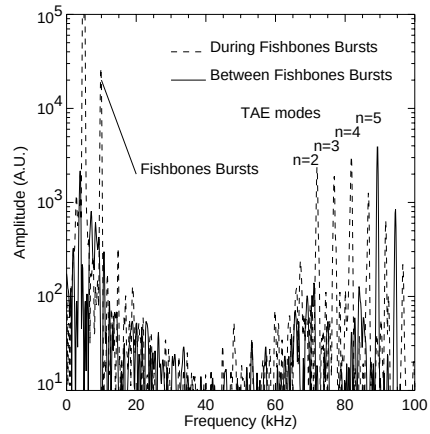

Figure 3.15 - TAE mode spectrum with different toroidal mode numbers (n), during the fishbone bursts and in between the fishbone bursts.

To observe the effect of the influx of tritons to its penetration to the plasma core, two different time dependent tritium density boundary conditions were used at the last closed flux surface: (i) a constant value of $n_T(a) = 5\times10^{15}$ m^3; (ii) varying from $n_T(a) = 5\times10^{15}$ m^{-3} up to $n_T(a) = 3\times10^{18}$ m^{-3}. During the tritium puff this boundary was decreased to its initial value 500 ms after the puff. In these simulations the plasma has been considered to be completely neo-classic without any anomalous contribution.

Figure 3.16 shows the results from the simulation. It is clear that the time between the starting of the gas puffing and the time that the neutron yield reaches its maximum, at the edge and the core channels, is longer for the simulation with non-constant boundary tritium density. The difference in the level of the reaction rate is also obvious for the case with a higher boundary density. The higher the tritium densities at the last closed flux surface, the lower is the out flux of particles (or even reverses the sign of the particle flux from positive to negative), keeping the tritium particles in the plasma core for a longer time.

The recycling (or reflection) coefficient R^{TT} is the least known parameter, which depends on the status of the wall and target plates. The best we can do is to study how sensitive is the result of our simulation with respect to a variation between $0 \le R^{TT} \le 0.9$ that is, R=0.0, R=0.5 and R=0.9. Figure 3.17 presents an increase of the neutron yield in all the plasma with the recycling and a smoothing of the initial ramp. The recycling change the tritium penetration by longer time to peak of the neutron yield and longer decaying time after it reaches its maximum. This is because there is a larger number of tritium particles that return back to the plasma, in other words the tritium stay longer inside of the plasma core. R = 0.5 leads the closet result to the experimental data.

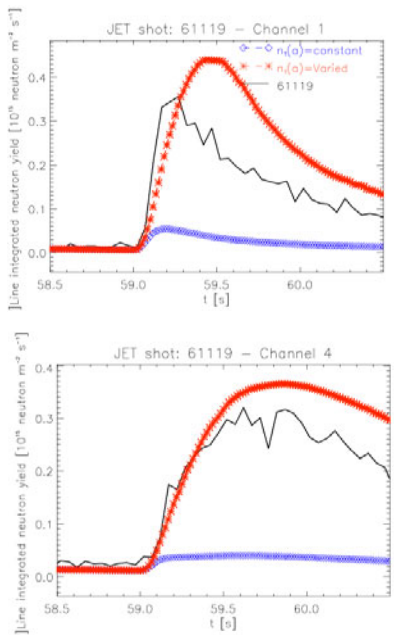

Figure 3.16 - Neutron yields horizontal camera for the edge channel (channel 1) and in the core channel (channel 4) for the two different time evolution of the tritium density at the last closed flux surface: a constant value of $n_T(a) = 5\times10^{15}$ m^{-3} (in blue) and varied boundary with the maximum value of $n_T(a) = 3\times10^{16}$ m^{-3} (in red), the experimental neutron yield for the pulse no. 61119 (in black).

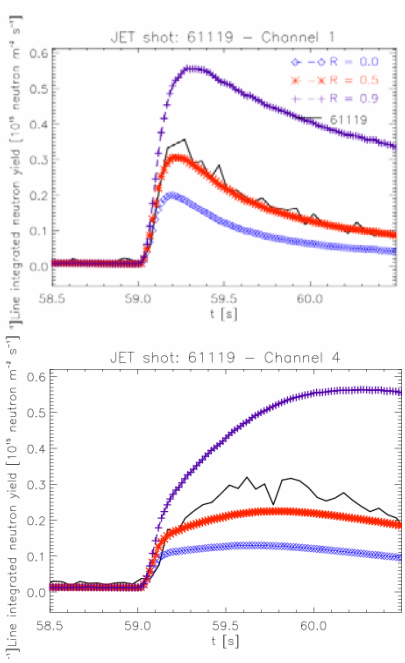

Figure 3.17 - Neutron yields horizontal camera for the edge channel (channel 1) and in the core channel (channel 4) for the three different recycling values: R = 0.0 (in blue), R = 0.5 (in red) and R = 0.9 (in purple).

3.3.9.2. Transport

(i) The ETB

In recent work with impurities it was shown that the neo-classical convective velocity for impurities changes sign from positive to negative when the edge deuterium density falls below the critical value. To take this effect into account, three different boundary values for the deuterium density have been prescribed. The neo-classical diffusion does not change significantly within the ETB for the different simulations. On the other hand the neo-classical convective velocity changes dramatically with the density gradient. The velocity is positive for the lower density gradient and it becomes negative for the higher density gradients.

(ii) The core

Three different tritium diffusion profiles neo-classical and two with additional anomalous contribution with different values of the anomalous multipliers of $c_T = 0.5$ and $c_T = 1.0$ were used to study the influence of the anomalous diffusion in the tritium penetration. It was found in the time to peak of the integrated neutron yield. The biggest difference was observed in the core channel. The time difference between the neo-classical diffusion and the highest level of the anomalous diffusion was around $\Delta t \cong 200$ ms. The neutron yield decay after it reaches the maximum is also faster for the highest diffusion.

(iii)Power deposition.

It was found that the higher is the plasma density the closer the tritium transport is to the neoclassical values. Nevertheless the tritium transport for pulses with ICRH had a higher anomalous contribution than the ones with NBI only. For example, in two consecutive JET pulses #61119 described above (Figure 3.17) and #61118 with 10.5 MW of NBI and 2.5 MW ICRH. The latter pulse had a higher density and lower temperatures but the best values of the anomalous transport coefficients for the particle diffusion and convective velocity were $c_T = 1.0$ and $c_{Tq} = 1.7$ comparatively, with #61119 that was $c_T = 0.5$ and $c_{Tq} = 0.0$. In these simulations only the NBI power deposition was considered. But simulations with the PION code demonstrated that the power is not going all to the electrons but mainly to the ions due to synergy effects. The results for different power deposition profiles are plotted in Figure 3.18 and it clearly indicates that the influence of ICRH should be taken into account, even when the power is low.

3.3.10. Neoclassic Tearing Modes (NTM) in hybrid regime

3.3.10.1. Triggering processes

In JET hybrid scenarios (HS) three types of triggering for the (3,2) NTM were observed: (i) as a (3,2) tearing mode

that started during the L-mode phase; (ii) during H-mode and in the presence of (1,1) modes; (iii) spontaneously during H-mode. During the L-mode, the collisionality regime is in the Pfirsch-Schlüter. In this regime the boostrap current is small and so the (3,2) mode can only be current driven and it is therefore probably triggered when the stability parameter Δ' is positive. The (3,2) mode becomes a NTM after the L to H-mode transition when the bootstrap current is significant. For the spontaneous NTMs, the (3,2) island growth rate was exponential, similar to those observed in low β_N plasmas where the onset coincides with the first sawtooth crash after the L to H transition.

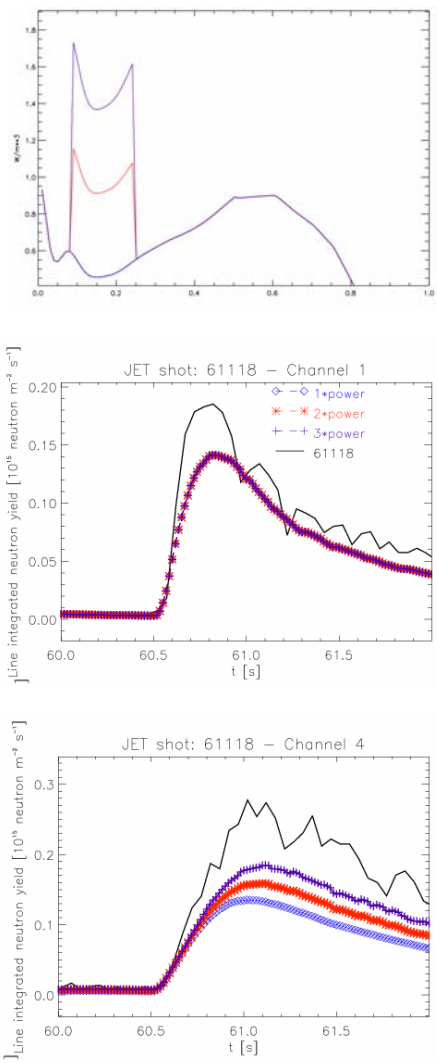

Figure 3.18 - a) Power deposition profile used in the simulations; b) the respective results and the experimental neutron yield for the pulse no. 61118.

The total number of pulses in the HS database was 48. In half of them neither the fishbone nor the sawtooth were observed and for these pulses q(0) > 1 was assumed. In all these pulses a (3,2) NTM was triggered. In the pulses, in which the (3,2) NTM was triggered spontaneously the shear is small at q = 1.5. In the other half of the pulses from the HS database (Figure 3.19), the q(0) ≤ 1 was assumed when, at least the fishbone instabilities were observed. In 12 of these pulses the (3,2) NTM was not observed but the sawtooth and the fishbone instabilities were present.

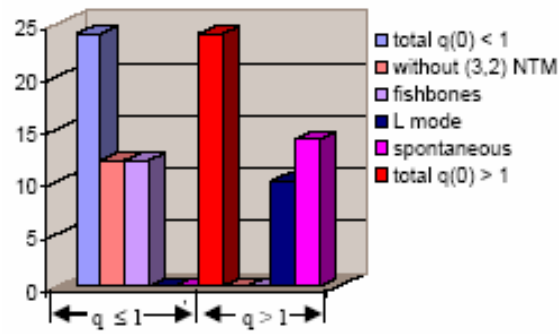

Figure 3.19 - Number of JET pulses in the hybrid scenario database for different types of (3,2) triggering

(ii) Energy confinement

In positive shear plasmas a reduction typically of 10-20 % in energy content is observed after the (3,2) NTM onset. The decrease in energy confinement is much lower for HS pulses (≤ 5%) the increase of confinement degradation with β_N is also lower. A possible explanation is the island width that is in average around 2 to 6 cm.

The island width is proportional to the square root of the magnetic perturbation for a constant shear and radius of the resonance surface. The island width is not only perturbed by the ELMs but also by the (4,3) NTM. Figure 3.20 shows that after the disappearance of (4,3) NTM, the (3,2) NTM grows to a saturated width and the core ion temperature decreases more than the core electron temperature.

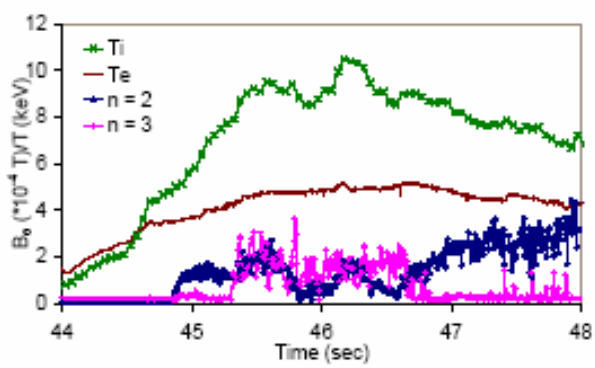

Figure 3.20 - Mode amplitude for the (3,2) NTM (blue), the amplitude of the (4,3) NTM for comparison (pink); electron temperature at R = 3.2 (brown); ion temperature at R = 3.14 (green) for the pulse # 60926.

3.3.11. Time–frequency analysis of nonstationary fusion plasma signals: comparison between the Choi –Williams distribution and wavelets

Recently, the Choi–Williams distribution has been effectively used to analyze nonstationary phenomena in fusion plasmas for which the spectrogram did not produce the best possible result. In principle, the Choi–Williams distribution is superior to wavelets, as it can yield excellent time–frequency resolution. Here, the advantages of using the Choi–Williams are shown using real fusion plasma signals. The comparison is for phenomena in JET, such as sawtooth (ST) crashes and neoclassical tearing modes (NTM) in discharges with ion cyclotron resonant heating (ICRH), and Alfvén cascades. In Figure 3.21, a ST crash appears as a broadband event at 60.6095 s, along with several modes including the (m =3, n =2) NTM at 5 kHz. In such a discharge with low β_N and ICRH, NTM may start with, or after the ST crash. So, good time–resolution is required. The time resolution of the spectrogram is not quite satisfactory, the region around the ST crash appearing blurred. The dependency of the time resolution of the scalogram on frequency is evident. In this case, for which good time resolution is important at all frequencies, the scalogram actually gives a worse representation than the spectrogram. The Choi–Williams distribution represents the modes and the ST crash with better time resolution than the spectrogram and the scalogram, although higher frequency modes appear somewhat masked by artifacts.

Using the Choi–Williams distribution is advantageous if the spectrogram fails to produce acceptable results, as long as the signal structure is not too complex, that is, with too many modes too close together in the time–frequency plane, so that artifacts can be adequately reduced. Wavelets, on the other hand, although sometimes improving upon the spectrogram, are unable to render sharp time–frequency representations as those produced by the Choi–Williams distribution.

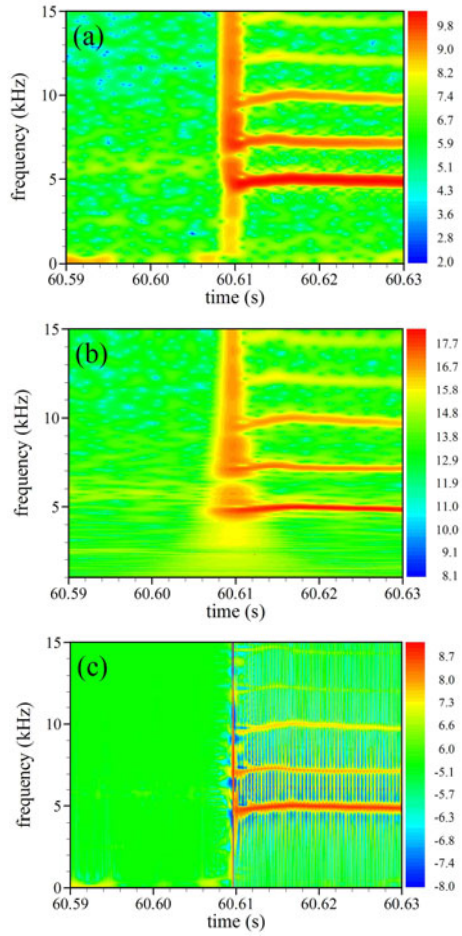

Figure 3.21 - Analysis of a magnetic pickup coil signal (JET pulse 50668), using (a) the spectrogram, (b) the scalogram, and (c) the Choi–Williams distribution.

3.3.12. Disruptions and runaway electrons in JET

Experiments and concurrent numerical modelling provided further contributions to the model for disruption generated runaway electrons (REs) in large tokamaks.

Limiter configuration with low elongated plasmas in JET enabled more stable behaviour of the runaway beams during and after disruptions resulting in long-lived runaway current plateaux (Figure 3.22). Interacting with cold post-disruption plasma RE beam produces detectable soft X-ray radiation providing information on evolution of runaway current-carrying channel in time and space. This data has been used in numerical modelling of the runaway process during disruptions.

A set of equations for the electron momenta (normalized to $m_e c$) together with evolution of runaway electron density has been solved at the initial conditions being inferred from the experimental data (plasma current, density, etc).

Experimental values of τ (characteristic current decay time) are concentrated in a range between 10 and 20 ms over a wide variation of the pre-disruption plasma currents. Calculations yield the values of post-disruption electron temperature $T_e \cong$ 10-15 eV at given plasma inductance $L_p \cong 4.5 \cdot 10^{-6}$ H. With these T_e values the numerical modelling provided close agreement between evolutions of the measured plasma current in disruption #63117 and total calculated current, which consists of two fractions: calculated runaway current (I_{RE}) and exponentially decayed resistive part (Figure 3.23(a)). Numerical simulations also show that the secondary avalanching process causes the dominating part of the disruption generated runaway electrons (Figure 3.23(b)). Depending on the initial conditions the current densities being inferred from calculated n_{RE} can achieve values up to $j_{RE} \cong 1$ MA/m^2.

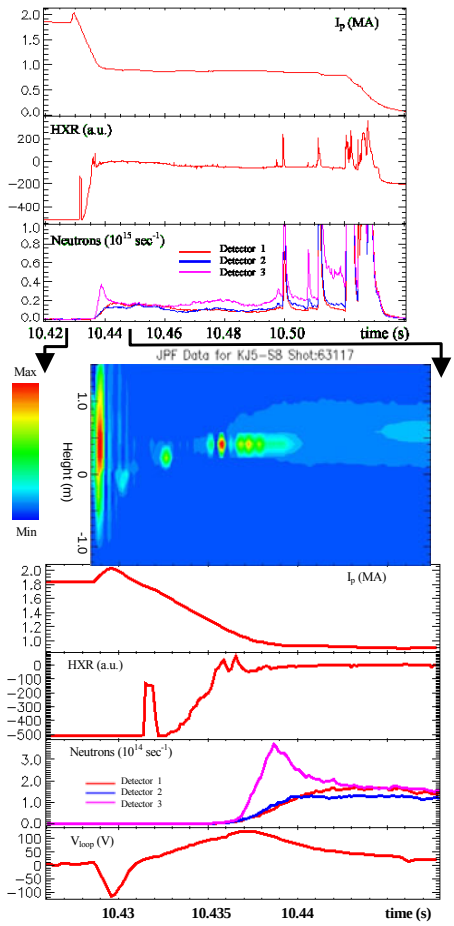

Figure 3.22 - Long-lived runaway electron beam generated at disruption #63117. Plasma currents (I_p), photo-neutron emission (Neutrons), Hard X-ray (HXR) and loop voltage (V_{loop}) signals are compared to the evolution of the soft X-ray emission (in arbitrary units).

The evolution of the test runaway electron in a momentum space and temporal evolution of RE density have been modelled in assumption that cross-section of RE current-carrying channel might have different size during current quench phase. Increase of RE current (as a result of larger beam cross-section) at other equal initial plasma and runaway generation parameters decreases the maximal RE densities and energies. Note, that close correspondence of the modelled and measured currents in Figure 3.23(a) has been obtained if the evolution of the cross-section size of RE current-carrying channel (as estimated from soft X-ray measurements) has been taken into account.

3.3.13. Effects of large magnetic islands on particle confinement trace-tritium studies–TRANSP modelling

The recent JET trace tritium campaign allowed us to study the effects of large magnetic islands induced by neo-classical tearing modes (NTMs) on tritium (T) particle transport. These kind of discharges are generally correlated

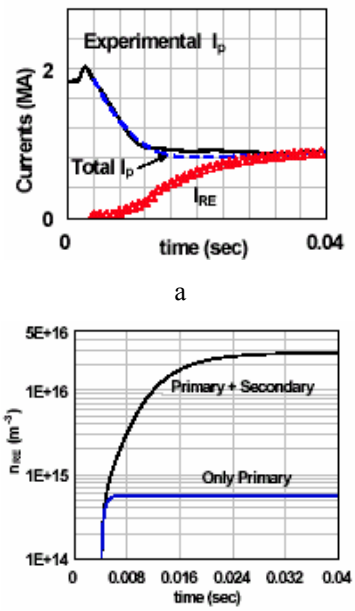

Figure 3.23 - Comparison of the measured plasma current to the calculated total current (RE current+plasma resistive current) at exponential decay of the resistive plasma current with characteristic time 0.01 sec (a). Calculated runaway electron density for primary only and for primary+avalanching mechanisms of runaway electron generation (b).

with an energy confinement degradation which could be related to the flattening the pressure around the magnetic islands. To quantify these effects transport studies were initiated using the suggested method proposed by the Task Force DT (TF-DT). Simulations with TRANSP were carried to estimate the two-dimensional profile of the neutron emissivity and the transport coefficients for neutrals, which are, then, used by the TF-DT to run the transport analysis package UTC. This code computes the T transport diffusion coefficient D_T and the relative pinch velocity V_T/D_T that best fits the experimental observation of the 2.5 MeV (D-D) and 14 MeV (D-T) neutron emission along 19 lines of sight.

Two trace tritium pulses, with and without NTMs have been modeled. Figures 3.24 and 3.25 show two-dimensional profiles of the 14 MeV neutron emissivities obtained by TRANSP for a given test T density profile. Similar simulations were done for each discharge for a set of 20 different T density profiles which are then used by UTC as a function basis for the T density. From the neutron emissivities given by TRANSP as a function of these T density profiles and the observable neutron emission, UTC estimates D_T and V_T/D_T profiles. Preliminary results suggest that the presence of magnetic islands can increase the T diffusion (D_T) in the plasma enclosed by the island and could reduce the T pinch velocity in the vicinity of the island (Figure 3.26).

However, since the majority of the 14 MeV neutron emission come from collisions between thermal T and D-beam, a more rigorous study requires further modeling because the effects of the magnetic island on the fast NBI ions were not yet taken into account.

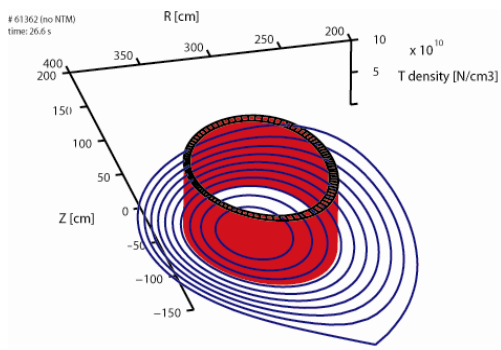

Figure 3.24 - 14 MeV neutron emissivity contours for the pulse #61362 (no NTM) using the given T density profile

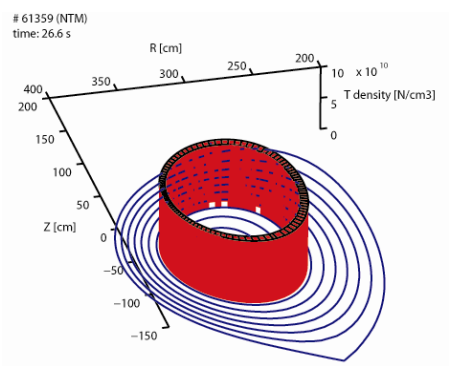

Figure 3.25 - 14 MeV neutron emissivity contours for the pulse #61359 (with NTM) using the given T density profile

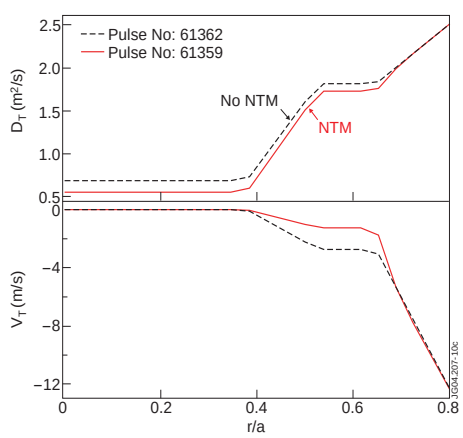

Figure 3.26 – UTC transport results for D_T and V_T for pulses #61362 (no NTM, black) and #61359 (with NTM, red)

3.3.14. On the cross-correlation between parallel and radial fluctuating velocities

The possible role of turbulence on the momentum re-distribution mechanisms in the plasma boundary region of tokamak plasmas was studied. Plasma profiles in the JET boundary plasma have been obtained using a fast reciprocating probe system that consists of arrays of Langmuir probes allowing the simultaneous investigation of the radial structure of fluctuations and parallel Mach numbers.

The contribution of the Reynolds stress term, $d<\tilde{v}_r\tilde{M}_{||}>/dr$, $\tilde{v}_r$ and $\tilde{M}_{||}$ being the fluctuating (ExB) radial velocity and the fluctuating parallel Mach number respectively, provides the mechanism to convert the turbulent scales (high frequency fluctuations) into a mean parallel flow. A comparison between the parallel flow profiles between forward and reversed field discharges is presented in Figure 3.27. In the forward field direction, (ion $B\times\vec{\nabla}B$ drift direction down towards the divertor), a strong parallel flow is measured at the top of the machine in the direction from the outer to the inner divertor. For reversed field, the measured flow is smaller but approximately symmetric with respect to a symmetry axis given by a positive offset. Figure 3.28 shows radial profiles of $<\tilde{v}_r\tilde{M}_{||}>$ obtained in forward and reversed field in the proximity of the LCFS in JET. In the plasma region where the floating potential becomes more negative (which turns out to be very close to the region where the perpendicular velocity shear is developed) there is evidence of significant radial gradients. It should be noted that the quadratic term of fluctuating velocities changes sign when the magnetic field is reversed.

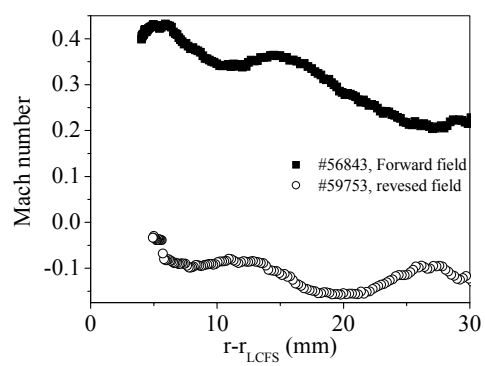

Figure 3.27 - Comparison of Mach number profiles between a forward and reversed toroidal field discharges in JET.

An estimate of the importance of turbulence in the evolution equation of the parallel flow requires a comparison of $d<\tilde{v}_r\tilde{M}_{||}>/dr$ with the magnitude of the parallel flows damped / driven by different mechanisms. The radial derivative of $<\tilde{v}_r\tilde{M}_{||}>$ was computed near the shear layer being its value in excess of $5\text{x}10^3$ s^{-1} both in

forward and reversed field in the JET tokamak. This result implies that, in the framework of our limited data base, the transport related momentum source ($n_e m_i \, d < \tilde{v}_r \tilde{v}_{\parallel} > / dr$) will be in the range of 1 – 5 N/m^3 in the JET boundary region, comparable with previous analysis of force balance which indicate a momentum source at the level of 10 N/m^3. Therefore, in the plasma edge, the Reynolds stress seems capable of sustaining a non- negligible parallel velocity.

This mechanism might be an ingredient to explain recent observations in Alcator C-mod showing that the toroidal momentum propagates in from the plasma edge, without any external source involvement. This mechanism can be particularly relevant during the L-H transition where the level of turbulence is mainly reduced near the edge. Then, radial gradients in the level of turbulence might develop, allowing a momentum redistribution (driven by internal-turbulent forces).

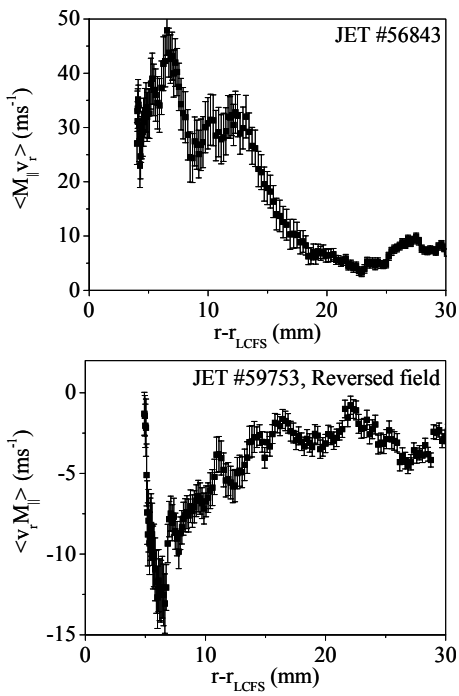

Figure 3.28 - Radial profiles of the cross-correlation between parallel and radial fluctuating velocities in JET L-mode plasmas near the LCFS in forward and reverse field discharges

3.3.15. Design of a new reciprocating probe head

A new reciprocating probe head has been designed to study momentum transport (Figure 3.29). The probe will be rather compact allowing the simultaneous measurement of the parallel flow at two radially separated positions, the radial and poloidal velocities and the fluctuations induced particle flux.

Concerning physics goals for the probe, the emphasis will be on the momentum re-distribution mechanisms driven by turbulence. Both the poloidal and parallel components of the momentum can be measured as well as the energy transfer between turbulence and parallel flows. The probe will also allow the continuation of the investigation in the dynamical relation between transport, radial electric fields, parallel flows and gradients.

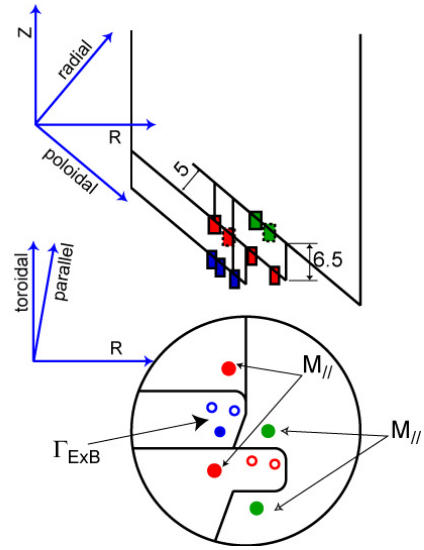

Figure 3.29 – Schematic illustration of the new turbulent transport probe head

3.3.16. Exploitation of the microwave reflectometry systems

3.3.16.1. ELMs studies

A study of the ELM activity using an X-mode correlation reflectometer (KG8b diagnostic) has been carried out. The 76-78 GHz channels (which generally probe the plasma edge region) are quite sensitive to the ELM activity (Figure 3.30). A drop of the signal amplitude as well as a significant increase of the fluctuations of the signal phase is observed during the ELMs. This result highlights that the loss of confinement during the ELMs is coupled with an increase of the turbulence. This is confirmed by the correlation reflectometry measurements on the bottom of the figure, which point out a significant drop of the correlation between the phases of two reflected signals at close frequencies, during the ELMs.

3.3.16.2. Turbulence studies

Spectral broadening induced by parametric instability in lower hybrid current drive experiments have been studied. Reflectometry measurements from the KG8b diagnostic showed an enhancement of the density fluctuation spectrum in the plasma edge region during the phase of injection of LHCD power. After the LHCD is switched on, a broadening of the spectrum of the reflected signal is observed (Figure 3.31).

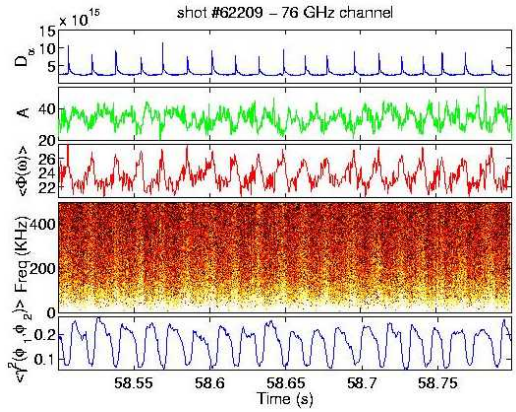

Figure 3.30 – Effects of type I ELMs on the X-mode correlation reflectometer data. From the top to the bottom: (a) Emission D_α displaying the ELM occurrence; (b) Amplitude of the reflected signal; (c) Averaged level of phase fluctuations of the reflected signal; (d) Spectrogram of the reflected signal phase; (e) Correlation between the reflected signal phases at two close frequencies (76 and 76.9 GHz)

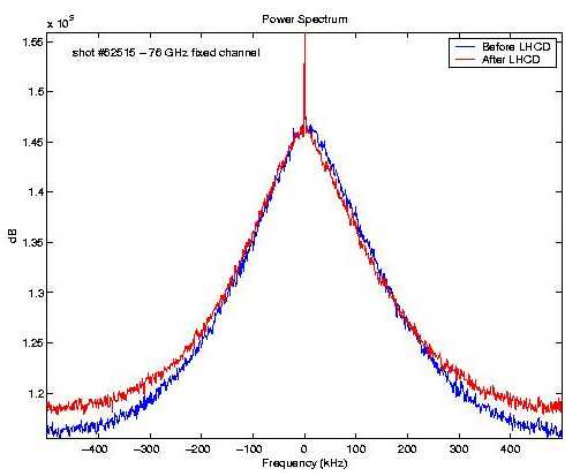

Figure 3.31 – Effect of the LHCD heating on a reflectometry signal of fixed frequency 76 GHz probing the plasma edge region.

The link between turbulence and plasma rotation is being investigated. A significant reduction of the turbulence was noticed when the cut-off layer of the reflectometry probing signal explores the ITB region associated with large negative poloidal velocity v_θ of plasma rotation. The spectrogram obtained from a sliding FFT of a reflected signal displays a reduction of signal fluctuations when the cut-off layer moves inner in the plasma where the ITB forms (Figure 3.32).

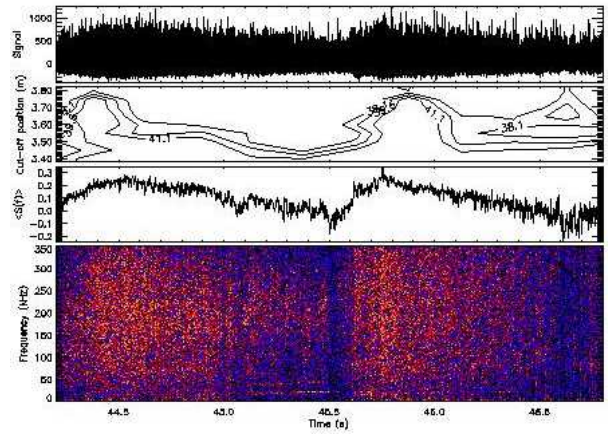

Figure 3.32 – Reduction of plasma turbulence in the ITB region observed from a reflectometry signal at fixed frequency 39.6 GHz. From the top to the bottom: (a) Raw reflected signal (b) Radial position of the cut-off layer (c) Averaged level of the reflected signal fluctuations (d) Spectrogram of the reflected signal.

3.4. PERFORMANCE ENHANCEMENTS

3.4.1. Introduction

IST/CFN was responsible in 2004 for four tasks of the JET Enhanced Performance Project:

- Mw Access-Project Management and Implementation;
- MPR-Project Design and Procurement Activities[2];
- TOF-Project Design and Procurement Activities[2];
- RTP-Development Real-time Test Facility.

Concerning the *Mw access – Project: management and implementation,* Dr. Luis Cupido has assured the coordination of the project, including the supervision of the commercial contracts. Test and measurement activities of the antenna cluster have been also carried out (Figure 3.33).

Figure 3.33 – MWA antennas delivered to JET in September 2004.

[2] Work in collaboration with the Association EURATOM/SKN

Regarding the *development real-time test facility*, transition from the initial design based on a System-On-Chip approach to a PC based system has been made. The schematic and layout design of the waveform generator (WG) PCI module prototype have been performed. One WG prototype board has been assembled and tested. Four final WG modules have been commissioned and tested. Firmware codes have been written for the development of the programmable logic devices, including the design, simulation and test of a CIC interpolator filter and sharpening FIR filter, both programmable in real-time. The low-level Digital Signal Processor (DSP) software has been implemented. A code for interfacing with the ATM real-time network has been developed. A complete PC based system with four waveform generator modules has been assembled. The Linux based control software, the Application Programming Interface (API) and the MDSPlus interface software have been developed.

Concerning the *MPR-Project: design and procurement activities* and the *TOF-Project: design and procurement activities,* two prototypes of the time digitizer (TD) module have been assembled and tested (Figure 3.34). A Matlab® data analysis program for automatic detection of functional and performance errors on TR has been developed. Six plus two spare TR boards as well as three TD boards have been assembled and tested at IST and sent to the Swedish EURATOM Association for integration on the MPRu and TOFOR diagnostics. The modules control and test software both for the Windows and Linux OS have been completed. Software and hardware manuals have been finished. IST/CFN staff has collaborate with VR on the integration of the modules in the diagnostics.

3.4.2. Real-time test facility

The test-bench system provides an analogue or digital replica of signals stored in a database, to generate stimulus for real-time control and data acquisition tools under test.

The on-site developed system (Figure 3.35), incorporating four DAC PCI modules, provides 32 analogue channels and one ATM link with the following main characteristics: (i) 32 analogue output channels with 16 bits resolution at up to 50 MSPS sampling rate; (ii) ±10 V output range on 600 Ω output impedance; (iii) 2 GByte of real-time signal storage capacity; (iv) includes four TMS320C6415 DSPs and four XC2V1500 FPGAs for real-time signal processing; (v) one full-duplex ATM optical port with 155 Mbps of transfer rate.

The software developed for the test-bench allows the integration with the JET MDSplus signal database server as well as with the Web server based Level-1 control interface with JET CODAS.

Figure 3.35 - Test-bench system.

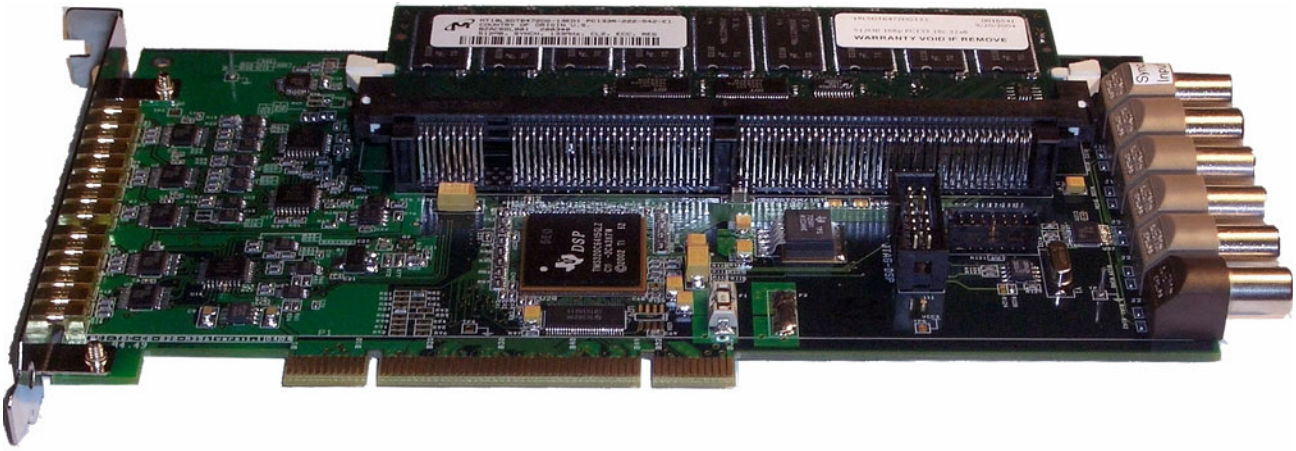

Figure 3.34 - Time digitizer module.